Rare Metal Materials and Engineering
Volume 51, Issue 2, February 2022
Available online at www.rmme.ac.cn

Science Press

Cite this article as: Jiang Jiayang, Du Jinghong, Yan Jikang, et al. Preparation of $Al_xCuFeNiCoCr$ High-Entropy Alloy by Powder Metallurgy Method and Its Properties[J]. Rare Metal Materials and Engineering, 2022, 51(02): 392-399.

ARTICLE

Preparation of $Al_xCuFeNiCoCr$ High-Entropy Alloy by Powder Metallurgy Method and Its Properties

Jiang Jiayang, Du Jinghong, Yan Jikang, Zhang Jiamin, Gan Guoyou

Faculty of Materials Science and Engineering, Kunming University of Science and Technology, Kunming 650093, China

Abstract: $Al_xCuFeNiCoCr$ high-entropy alloys were prepared by powder metallurgy method. The effect of Al content on the properties and microstructure of the alloys was studied, and the change in the grain properties during the preparation of the alloys was discussed. The results show that the alloy grains are refined during the milling process, and the grain size of the alloy increases with the increase of Al content. New grains are generated in the alloy during the sintering process, and an intermetallic compound containing Al is initially formed by absorbing a certain amount of heat. A phase with simple crystal structure is obtained after heating at 1200 °C for 2 h, which confirms the formation of high-entropy alloy. Based on the obtained energy spectrum, the alloy composition is uniform, and the alloying degree is high. However, with the increase in Al content, a small number of high-contrast areas with high Al content emerge. The alloys exhibit a good high-temperature oxidation resistance and electrochemical corrosion resistance. The oxidation resistance at high temperature increases with the increase of Al content. The self-corrosion voltage is −235 mV when x=1.0. With the increase in Al content, the hardness also increases. The best overall properties of the alloy are achieved when x=1.0.

Key words: high-entropy alloys; powder metallurgy; electrochemistry

In recent years, due to the continuous pursuit of performance, the traditional alloy materials have gradually failed to meet the performance requirements, and new materials are extensively sought to achieve a breakthrough in this area. As a new type of alloy material discovered in the last two decades, high-entropy alloys have received considerable attention because of their unique composition[1,2], excellent corrosion resistance[3,4], and mechanical properties[5]. High-entropy alloy mainly refers to an alloy prepared and formed by a variety of elements with equal molar ratio. The mixing entropy of the alloy is higher than 1.61R (R is the gas constant) [6]. Therefore, the properties of high-entropy alloys are determined by all the constituent elements[7]. Based on its alloy design, the high-entropy alloy can be regarded as a super solid solution[8,9]. Solute and solvent cannot be distinguished in the alloy. The crystal structure of high-entropy alloys usually forms a body-centered cubic (bcc) structure or a face-centered cubic (fcc) structure. At the same time, due to the interaction between each component element in the solid solution, the growth of crystal nuclei is inhibited to a certain extent, and small crystal structure phases are readily formed[10,11]. In recent years, high-entropy alloys are mainly used to prepare thin films and bulk materials. Thin films are mostly prepared by thermal spraying and vapor deposition[12-14]. Bulk materials are predominantly prepared by mechanical alloying and arc smelting[15-17]. At present, the main synthetic method for high-entropy alloys is arc smelting. This method experiences restrictions in large scale production, since the scale is limited by the possible crucible size[18,19]. A further challenge in arc smelting engineering pertains to the different properties of each element, which can result in different diffusion degrees for each alloy component. High-entropy alloys prepared under the same conditions exhibit different microstructures and poor reproducibility, as well as excessive energy consumption[20-22]. In this work, a combination of mechanical alloying and powder metallurgy processes including compression and sintering was employed in the preparation of high-entropy alloy samples. By studying the relationship between mechanical properties and microstructure, the influence of Al content on the alloy properties was explored.

Received date: February 08, 2021
Corresponding author: Du Jinghong, Ph. D., Professor, Key Laboratory of Advanced Materials of Yunnan Province, Faculty of Materials Science and Engineering, Kunming University of Science and Technology, Kunming 650093, P. R China, E-mail: cldjh@sina.com

1 Experiment

A series of $Al_xCuFeNiCoCr$ high-entropy alloys were prepared by powder metallurgy methods. Pure elemental powders of Al, Co, Cr, Fe, Cu, and Ni (99.9 % purity, Alfa Aesar) with particle sizes less than 60 μm were used as raw materials. The materials were weighed according to the molar ratio of Al: Cu: Fe: Ni: Co: Cr=x: 1: 1: 1: 1: 1 to synthesize five different alloys with x=0, 0.5, 1.0, 1.5, 2.0. The mechanical alloying process was conducted in a XQM-2A mill (TENCAN, China) with a rotation speed of 300 r/min for 6 h at room temperature. Agate balls with different diameters (10.8, 8.2, 5.2 mm) were placed into the agate pot with the original powder mixture. The ball to powder mass ratio was 6: 1. The milling operation was performed under a positive pressure of argon to prevent foreign substances from entering. To avoid an excessive temperature rise in the equipment, milling was paused for 10 min after each operating cycle of 60 min. A Mastersizer 2000 laser particle size analyzer (Malvern Panalytical Ltd, UK) was used to determine the particle size of the milled powders. The milled powders were compacted by YP-60T tablet press (JFL, China) using a tablet mould with diameter size of 12.8 mm under a uniaxial pressure of 600 MPa for 10 min. The pressed samples were sintered under vacuum (0.03 Pa) at 1200 °C for 2 h.

A 3H-2000PM Brunauer Emmett Teller (BET) surface area analyzer (BeiShiDe, China) was used to determine the pore volume, pore size, and specific surface area of the samples. Differential scanning calorimetry (DSC), performed on a NETZSCH STA 449 F3 Jupiter® thermal analyzer (NETZSCH-Geräte-bau GmbH, Germany) was used to measure the phase transition temperature and energy change under vacuum. Energy-dispersive spectroscopy (EDS) was carried out on a JSM-6510 scanning electron microscope (SEM, JEOL Ltd, Japan) to determine the metal element content. The SEM and an XPL-1503 reflected illumination polarization microscope (Lissview, China) were used for morphological and microstructural investigation of the powdered and block specimens. For X-ray diffraction (XRD) spectroscopy, a D8 advance X-ray diffractometer (Bruker, USA) with Cu Kα radiation was used to collect the X-ray diffraction patterns of the samples with a step size of 0.04 and a scanning speed of 5°/min. A X'pert diffractometer (Malvern Panalytical Ltd, UK) with Cu Kα radiation equipped with a HTK-2000N high-temperature chamber (Anton Paar GmbH, Austria) with a step size of 0.03 and a scanning speed of 1.5°/min was used for XRD experiments at high temperatures. Microhardness profiling in sintered samples was carried out by a HMAS-D5SZ Vickers microhardness tester (WHW, China) under a load of 1 N with a residence time of 10 s. The average hardness was calculated based on fifteen random hardness determinations. A DH7000 electrochemical workstation (Jiangsu Donghua Analytical Instruments Co., Ltd, China) was employed for the determination of the corrosion resistance with 3.5wt% salt water as electrolyte, platinum and calomel electrode, corrosion potential from −0.6 V to 1.2 V, and a scanning speed of 0.001 $V \cdot s^{-1}$. The high temperature cycle oxidation resistance of the samples was studied at 600 °C using a muffle furnace. A ZEISS Sigma 500 field emission scanning electron microscope (FE-SEM, Carl Zeiss AG, Germany) was used to scan the element distribution in cross sections.

2 Results and Discussion

The specific surface area, pore volume, and pore diameter of the $Al_{1.0}CuFeNiCoCr$ high-entropy alloy before and after ball milling are listed in Table 1. The reduction in specific surface area after ball grinding indicates that fracture of the original skeleton and powder adhesion occur during ball milling. The decrease of pore volume and the increase of pore size indicate an increase in the proportion of large holes in the alloy, which further proves the occurrence of powder adhesion. Powder adhesion is mainly caused by Co and Al. While Al reacts readily with other elements during ball milling to form intermetallic compounds[23], Co is conducive to form a block body and also acts as an adhesion agent, which then promotes powder adhesion[24,25]. Furthermore, a recrystallization process may occur due to the formation of intermetallic compounds during the ball milling process.

To investigate the occurrence and extent of a recrystallization process, the grain size and the crystal structure of the alloy powder were determined by XRD before and after ball milling. Referring to Fig.1, the peak at 2θ=38.5°, assigned to the (111) Al plane of the fcc structure, is almost completely absent after ball milling. The same observation can be made for the small peaks of other elements at 2θ>70°. The result indicates that Al reacts with other elements in the alloy to form intermetallic compounds or dissolve other elements to form a solid solution structure[26]. While no new peaks are observed after ball millng, and the intensity of the peaks at 43.8° and 44.5° is decreased by 60%, which indicates a loss of crystallinity. However, the calculation of the degree of crystallinity using the software program Jade6[27] reveals that the crystallinity before ball milling is 45.18% and increased by 26.3% to 57.09% after ball milling. Therefore, one can conclude that a preferred orientation growth occurs during the ball milling process. Since the height of diffraction peaks decreases and no new diffraction peaks emerges, one can assume that the formed crystal structure causes systematic extinction in the XRD pattern.

The XRD patterns of the $Al_xCuFeNiCoCr$ powders after

Table 1 Specific surface area of $Al_{1.0}CuFeNiCoCr$ alloy powder

Powder sample	Specific surface area/$m^2 \cdot g^{-1}$	Pore volume/$mL \cdot g^{-1}$	Pore diameter/nm
Before ball milling	0.9794	0.0040	16.34
After ball milling	0.2268	0.0016	28.22

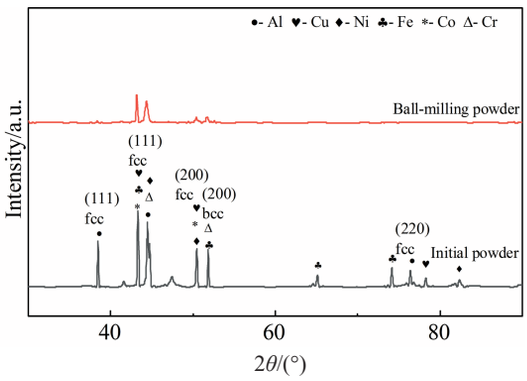

Fig.1 XRD patters of $Al_{1.0}CuFeNiCoCr$ powder before or after ball milling

ball milling are shown in Fig.2. The diffraction peak from the aluminum crystal surface (111) located at about 2θ =38.5° increases in intensity with the gradual increase of Al content. This indicates that the energy generated by the collision is limited, and Al does not completely react during the ball milling process under the employed ball milling parameters[28], and a small amount of Al remains in the alloy powder. At the same time, the diffraction peaks of the alloy at 43.8° and 44.5° are slightly widened with the increase of Al content, indicating that the formation of the alloy with (111) crystal face is promoted by the increase of Al content. Fig. 3 shows the change of the average particle size of the mixed powders before and after ball milling based on XRD. The particle size declines sharply after ball milling, and the particle size first decreases, then increases gradually with the increase of Al content. This indicates that the original skeleton is destroyed and new grains form during the ball milling process, and grain growth is promoted with the increase of Al content.

Sintering is one method of forming alloy blocks. To investigate the structural changes in the sintering process, DSC was carried out on a $Al_{1.0}CuFeNiCoCr$ block after ball milling. Referring to the TG-DSC curves in Fig.4, a mass loss of 0.99% can be observed between 91 and 746 °C followed by a mass increment of 0.52% between 746 and 968 ° C. The

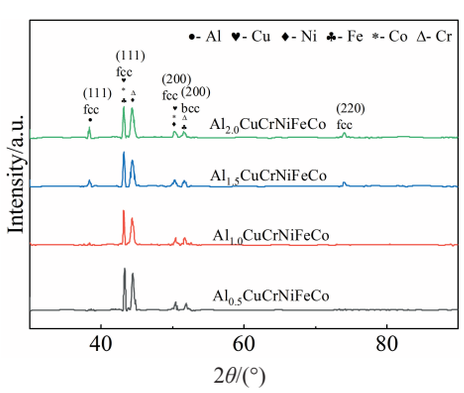

Fig.2 XRD patterns of $Al_xCuFeNiCoCr$ (x=0.5, 1.0, 1.5, 2.0) alloy powders after ball milling

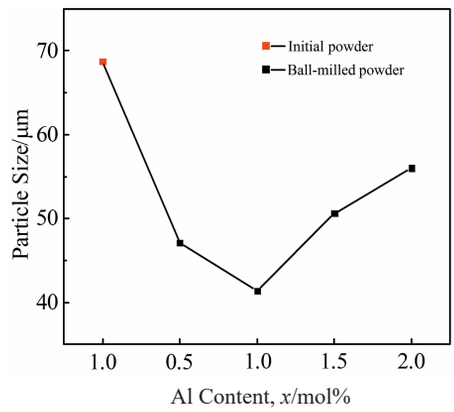

Fig.3 Mean particle size of $Al_xCuFeNiCoCr$ (x=0.5, 1.0, 1.5, 2.0) mixed powders before and after the ball milling

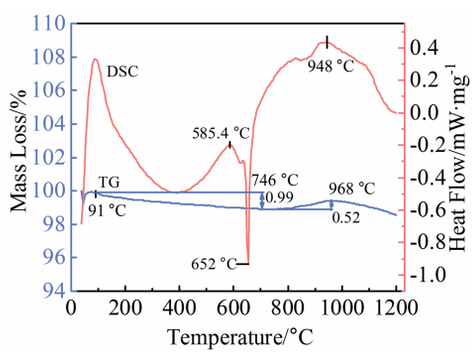

Fig.4 TG-DSC curves of $Al_{1.0}CuFeNiCoCr$ block after ball milling

mass loss may be caused by lubricant volatilization in the alloy during the pressing process. The mass increase can be explained by a reaction of volatile gases with the alloy surface or may be due to experimental errors. In summary, the alloy powder contains little volatile impurities, and the alloy block exhibits a good degree of compactness. The observation of a heat absorption peak starting at 585 ° C and reaching the maximum at 652 °C may be attributed to Al in the alloy block and to the fact that its intermetallic compounds absorb heat in this temperature range to form a localized melt. Since a crystal transformation is typically an exothermic phenomenon[29], a small exothermic peak appearing at 948 °C can be ascribed to a crystallization transformation caused by the interaction between each component in the alloy.

Based on the TG-DSC analysis results, the temperatures for in-situ high-temperature XRD experiments were chosen for a $Al_{1.0}CuFeNiCoCr$ block after ball milling. Fig. 5 shows the XRD patterns at the selected temperatures, and the bottom line refers to the XRD pattern of the block at 1200 °C for 2 h. When the temperature reaches 584 °C, a new diffraction peak emerges at 2θ=38°, and the intensity of the diffraction peak increases with the increase of temperature. The appearance of the new diffraction peaks is mainly due to the initial reaction of Al with other components in the alloy. According to XRD analysis, $AlNi_3$ mainly forms at the beginning, which is

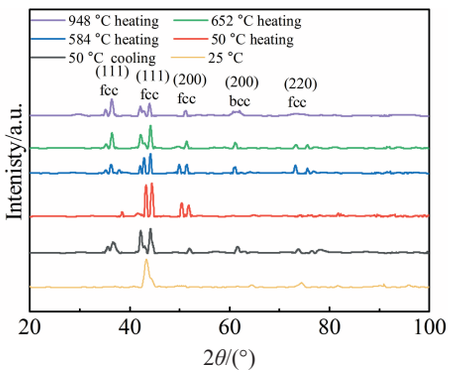

Fig.5 In-situ high-temperature XRD patterns of $Al_{1.0}CuFeNiCoCr$ block after ball milling

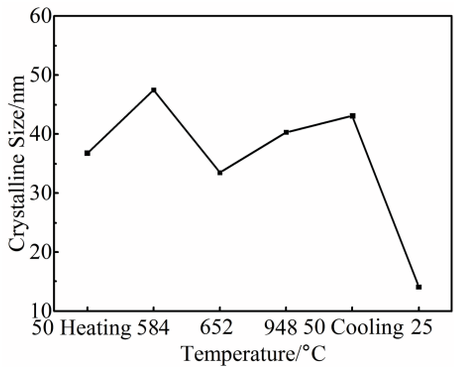

Fig.6 Variation of grain size with temperature in sintering process

consistent with the previous study, i.e. Al and Ni will be the first elements to react[30]. Furthermore, a series of diffraction peaks and a wide diffraction peak form at about 2θ=38° and 2θ=44.3° after cooling to 50 °C, which may be caused by the lack of long-time heat preservation during the experiment, resulting in incomplete reaction. After cooling, the diffraction peak at 2θ =38° decreases in intensity, indicating that the compound initially formed by Al constantly reacts with other alloy components. Moreover, the diffraction peak at 2θ=44.3° increases in intensity and broadens, indicating that some products responsible for this peak are generated. In the XRD spectrum at 25 °C, the diffraction peak at about 2θ=38° is absent, indicating that proper holding time is crucial in the sintering process. A sufficient holding time at the sintering temperature allows the atoms in the alloy to diffuse evenly, resulting in a higher degree of alloying. The spectra indicate that an alloy with a simple crystal structure is prepared, which possesses a typical property of a high-entropy alloy[31]. As indicated by a previous study, the fcc phase forms readily when the Al content is similar to the Ni content[32]. Therefore, bcc phase is less prominent than fcc phase in sintering process. The diffraction peak decreases with increase of temperature, which may be caused by grain growth or the formation of new grains. Therefore, we further analyzed the XRD pattern and calculated the grain size at different temperatures, as shown in Fig. 6. The grain size increases at the beginning and then decreases at about 652 °C, which can be attributed to initial grain growth and subsequent reaction of Al with other components, resulting in the formation of new grains in the alloy and the decrease of grain size. This observation is consistent with the XRD pattern. Furthermore, the grain size is larger after cooling, because due to a slower furnace cooling rate, grain growth is more prominent and results in a larger final grain size. The grain size calculation results of the 25 °C sample are small, indicating that the grain growth phenomenon is not obvious when the holding time for heat preservation is appropriate. At the same time, the grain nucleation of the alloy is more pronounced due to element diffusion, resulting in a smaller grain size.

According to alloy solid solution theory, a solid solution will be formed more likely and intermetallic compounds will be generated less likely with decreasing difference in atomic size and electrochemical properties[33]. To apply this theory on the alloys prepared in this investigation, the relevant characteristic parameters of the alloy elements are listed in Table 2, which indicate that the electronegativity and atomic size differences are not significant, theoretically supporting the formation of a solid solution. To study the microstructure and morphology of the sintered $Al_xCuFeNiCoCr$ alloys, the respective micro-images were recorded and are displayed in Fig. 7. A few pores are present in the alloy. A few areas with high contrast are visible when the Al content is high. The high-contrast region is mainly distributed around the alloy pores and does not appear in the matrix. To determine the distribution of elements in different regions with high contrast in the alloy, EDS analysis was carried out on the $Al_{2.0}CuFeNiCoCr$ alloy block with the largest regions of high contrast. The results are shown in Fig. 8 and listed in Table 3. The regions with high contrast mainly have high Al content and low Cr content, while the Cu content in the matrix is relatively low. Table 3 declares that the high contrast region is due to changes in Al content. Based on previous study, Cu is conducive to aggregation between dendrites and Cr in dendrites[26]. Therefore, the observation of low Cu content and low Cr content may be explained by segregation. The high Si content at point 3 is caused by sandpaper used during polishing. Because the test points are near the holes, point 2 and point 3 exhibit high O content.

Based on the XRD pattern, the alloy phase is characterized by a simple crystal structure. To determine the distribution of

Table 2 Relevant characteristic parameters of alloying elements

Element	Crystal structure	Melting point/°C	Electronegativity	Atomic radius/nm
Al	fcc	660	1.61	1.43
Fe	bcc	1535	1.83	1.27
Cr	bcc	1857	1.66	1.27
Co	hcp	1495	1.88	1.26
Ni	fcc	1453	1.91	1.24
Cu	fcc	1083	1.90	1.28

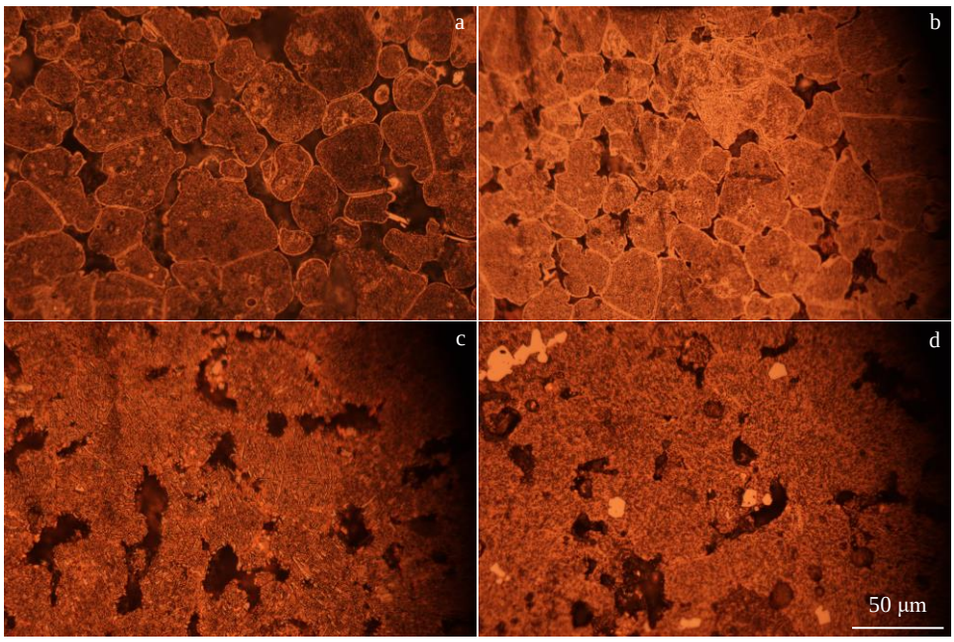

Fig.7 Microstructures of Al_xCuFeNiCoCr alloys: (a) $Al_{0.5}$CuFeNiCoCr, (b) $Al_{1.0}$CuFeNiCoCr, (c) $Al_{1.5}$CuFeNiCoCr, and (d) $Al_{2.0}$CuFeNiCoCr

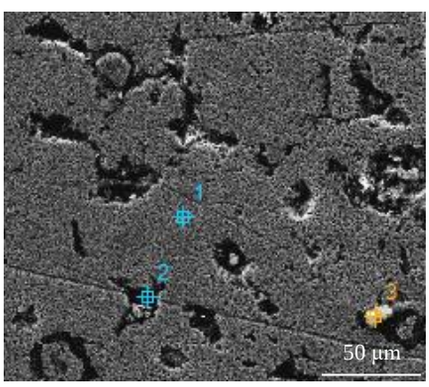

Fig.8 Microstructure of $Al_{2.0}$CuFeNiCoCr

Table 3 EDS results of points 1, 2, 3 marked in Fig.8 (at%)

Point	C	O	Al	Si	Cr	Fe	Co	Ni	Cu
1	2.23	3.47	28.42	0.56	15.89	14.44	14.7	15.56	12.74
2	23.51	47.09	11.71	1.87	2.87	3.08	3.23	3.21	3.44
3	18.76	42.47	10.53	11.20	1.88	4.04	3.78	3.38	3.96

elements in the alloy components, the uniformity of the components, and the degree of alloying, EDS analysis was carried out. Referring to Fig. 9, the distribution of elements is very uniform, and there is no obvious element aggregation. The microstructure of the alloy is more uniform after sintering. Furthermore, based on the semi-quantitative analysis of the total energy spectrum in Fig. 9h, the relative content ratio of each element is close to the preset ratio of the alloy. Therefore, the alloying degree is high, and the microstructure is uniform.

High-entropy alloys are generally characterized by good high-temperature stability, while a certain amount of pores are present in the samples prepared by powder metallurgy methods. To study the effects of pores on high-temperature stability, we examined the oxidation resistance of high-temperature cycling. Fig. 10 shows the relationship between the oxidation mass gain per unit area of the alloy and the time of burning the high-entropy alloy in air at 600 ° C. The oxidation kinetic curves demonstrate similar characteristics, roughly showing a parabolic shape. Initially, the oxidation process is intense, and the mass gain is fast. After oxidation for 6 h, the mass gain rate decreases significantly, which can be explained by the rapid formation of oxide film on the surface of the alloy in the initial oxidation stage; with increasing time, the thickness of the oxide film increases, which prevents the oxidation reaction to a certain extent; with the decrease of oxygen partial pressure at the interface, the oxidation reaction changes from direct contact reaction of alloy elements to ion diffusion reaction, which results in a decrease of the oxidation rate. It is also observed that the oxidation rate decreases with the increase of Al content when x is between 0.5 and 2.0, which indicates that Al contributes to the oxidation resistance of the alloy. With the increase of Al content, a thick Al_2O_3 oxide film readily forms on the surface of the alloy. A previous study confirms the high density of Al_2O_3 oxide film[34]. Consequently, the oxidation rate of the alloy is low, and the degree of oxidation is diminished. In summary, the high-entropy alloy prepared by powder metallurgy methods contains a certain amount of holes, but since pores have little effect on the high-temperature oxidation of the alloy, the pores might be closed.

Since the alloys demonstrate a certain corrosion resistance during the metallographic corrosion experiments, potentiodynamic polarization measurements were conducted. Fig. 11 shows the dynamic potential polarization curves of the

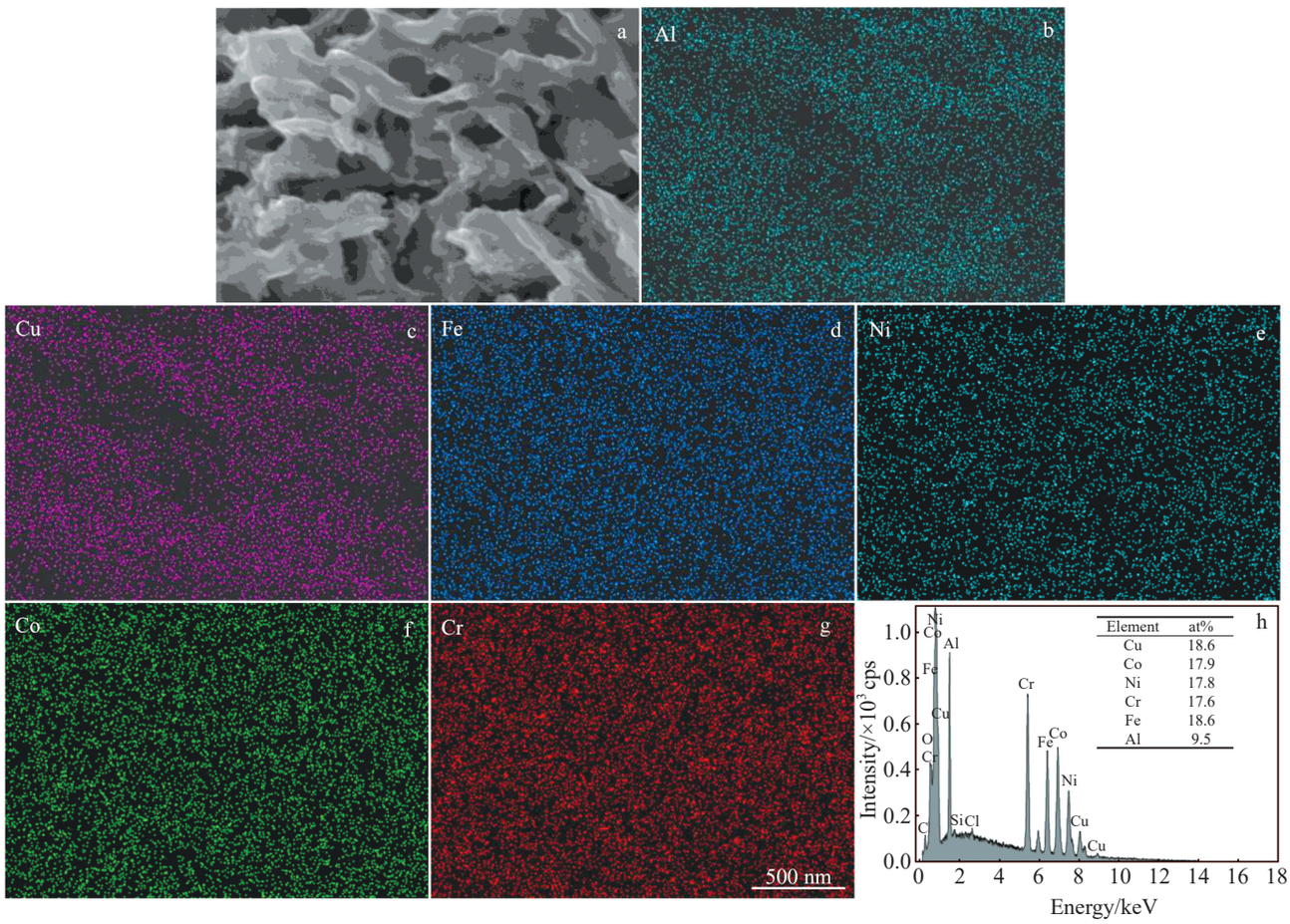

Fig.9 SEM micrographs showing the representative lamellar microstructure of $Al_{0.5}CuFeNiCoCr$ powder (a); EDS element mappings (b~g) and EDS results (h)

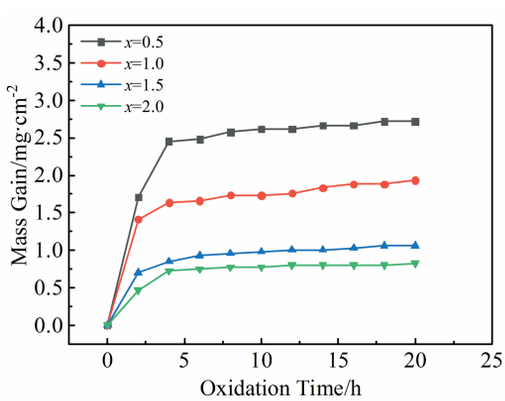

Fig.10 Oxidation kinetic curves of $Al_xCuFeNiCoCr$ (x=0.5, 1.0, 1.5, 2.0) in air at 600 °C

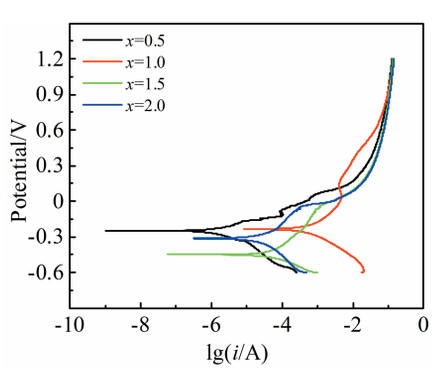

Fig.11 Polarization curves of $Al_xCuFeNiCoCr$ (x=0.5, 1.0, 1.5, 2.0)

$Al_xCuFeNiCoCr$ high-entropy alloys. The self-etching potential E_{corr} and self-etching current density I_{corr} of the samples calculated from the polarization curves are listed in Table 4. The four curves in Fig.11 have no obvious corrosion passivation area. With the change of Al molar ratio, E_{corr} and I_{corr} change considerably. At x=0.5, some fluctuations occur in the anodic polarization curve, which is caused by the intrusion of a small amount of electrolyte solution during the polarization process. With decreasing the (negative) E_{corr} value, the corrosion tendency increases, and with increasing I_{corr} value, the corrosion rate of the alloy increases[35]. Therefore, based on the E_{corr} values, the alloy exhibits the lowest corrosion tendency when x=1, and the highest corrosion tendency when x=1.5. Based on the I_{corr} values, the corrosion rate is the lowest when x=1 and the highest when x=0.5. In summary, $Al_{1.0}CuFeNiCoCr$ exhibits the best corrosion

Table 4 Electrochemical performance data of polarization curves of $Al_xCuFeNiCoCr$ (x=0.5, 1.0, 1.5, 2.0)

Sample	E_{corr}/mV	I_{corr}/×10^{-5}A·cm^{-2}
$Al_{0.5}CuFeNiCoCr$	-247	5.732
$Al_{1.0}CuFeNiCoCr$	-235	2.858
$Al_{1.5}CuFeNiCoCr$	-449	4.171
$Al_{2.0}CuFeNiCoCr$	-313	4.258

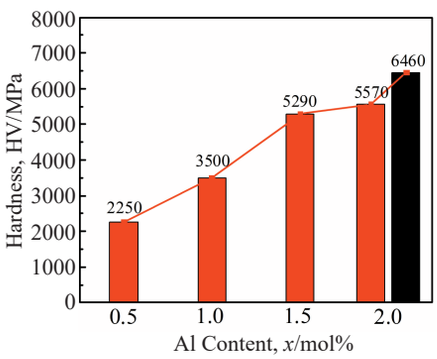

Fig.12 Microhardness of sintered $Al_xCuFeNiCoCr$ (x=0.5, 1, 1.5, 2)

resistance in the investigated series of alloys.

Fig. 12 shows the microhardness of $Al_xCuFeNiCoCr$, in which the red columns refer to the matrix hardness and the black column to the hardness of the high-contrast area. According to the results, the hardness increases with the increase of Al content, which can be explained by the solid solution strengthening effect and the lattice distortion effect with increase in Al content. Furthermore, the increase of Al content will promote the formation of bcc phase. bcc phase with higher Al content has higher strength and hardness than fcc phase, and consequently, the hardness of the alloy increases. It can also be observed that with increasing the Al content, the hardness increases faster at first, and then increases slowly. One can state that the main reason for this observation is that the solution strengthening reaches a peak value with the increase of Al content, a large number of second phase particles are precipitated in the alloy, and the dispersion strengthening gradually contributes to strengthening to a greater extent. Because of the diminishing strengthening mechanism, the strengthening effect is reduced. The hardness of the high-contrast region is higher than that of the matrix because of a higher oxide content in the matrix.

3 Conclusions

1) In the process of ball milling of $Al_xCuFeNiCoCr$ high-entropy alloys, the mechanical alloying reaction occurs, the powder mixing is more uniform than before ball milling, and the grain size becomes smaller. The increase in Al content requires a longer milling time to promote the reaction of the alloy.

2) In the sintering process, the intermetallic compound initially formed from Al is demonstrated by the presence of an endothermic peak in the DSC spectrum. After sintering, the alloy exhibits a simple crystal structure, and the elements in the matrix are evenly distributed.

3) The pores on the surface of the alloy are mainly closed ones, and the $Al_{2.0}CuFeNiCoCr$ alloy demonstrates the best high-temperature oxidation resistance. The $Al_{1.0}CuFeNiCoCr$ alloy demonstrates the best corrosion resistance.

4) The hardness of the alloy increases with increasing Al content. When the solution strengthening effect reaches the maximum, dispersion strengthening starts to play a greater role.

References

1 Laplanche G, Kostka A, Reinhart C *et al. Acta Materialia*[J], 2017, 128: 292
2 Li Zhiming, Tasan C C, Pradeep K G *et al. Acta Materialia*[J], 2017, 131: 323
3 Zhu Dezhi, Wu Jipeng, Liu Shiwen. *Rare Metal Materials and Engineering*[J], 2020, 49(11): 3875 (in Chinese)
4 Shi Yunzhu, Yang Bin, Xie Xie *et al. Corrosion Science*[J], 2017, 119: 33
5 Zhang Zijiao, Sheng Hongwei, Wang Zhangjie *et al. Nature Communications*[J], 2017, 8: 14 390
6 Gorsse S, Hutchinson C, Goune M *et al. Science and Technology of Advanced Materials*[J], 2017, 18(1): 584
7 Huang Hailong, Wu Yuan, He Junyang *et al. Advanced Materials* [J], 2017, 29(30): 7
8 Li Yanchao, Li Laiping, Gao Xuanqiao *et al. Rare Metal Materials and Engineering*[J], 2020, 49(12): 4365 (in Chinese)
9 Lei Zhifeng, Liu Xiongjun, Wu Yuan *et al. Nature*[J], 2018, 563(7732): 546
10 Li Ziyong, Fu Liming, Peng Jian *et al. Materials Characterization*[J], 2020, 159: 109 989
11 Patnamsetty M, Saastamoinen A, Somani M C *et al. Science and Technology of Advanced Materials*[J], 2020, 21(1): 43
12 Tong Y, Chen D, Han B *et al. Acta Materialia*[J], 2019, 165: 228
13 Wu Shiwei., Wang Gang, Wang Qing *et al. Acta Materialia*[J], 2019, 165: 444
14 Li Ruidi, Niu Pengda, Yuan Tiechui *et al. Journal of Alloys and Compounds*[J], 2018, 746: 125
15 Luo Hong, Zuo Shiwen, Li Zhiming *et al. Acta Materialia*[J], 2019, 164: 400
16 Luo H, Li Z, Mingers A M *et al. Corrosion Science*[J], 2018, 134: 131
17 Ikeda Y, Grabowski B, Koermann F. *Materials Characterization* [J], 2019, 147: 464
18 Long Yan, Zhang Weihua, Peng Liang *et al. Rare Metal Materials and Engineering*[J], 2020, 49(11): 3841 (in Chinese)
19 Bala P, Gorecki K, Bednarczyk W *et al. Journal of Materials Research and Technology*[J], 2020, 9(1): 551

20 Moravcikova-Gouvea L, Moravcik I, Omasta M *et al. Materials Characterization*[J], 2020, 159: 110 046
21 Cai Y, Zhu L, Cui Y *et al. Materials Characterization*[J], 2020, 159: 110 037
22 Harrington T J, Gild J, Sarker P *et al. Acta Materialia*[J], 2019, 166: 271
23 Batchelor T A A, Pedersen J K, Winther S H *et al. Joule*[J], 2019, 3(3): 834
24 Luo Shuncun, Zhao Chunyang, Su Yue *et al. Additive Manufacturing*[J], 2020, 31: 100 925
25 Huang Xi, Gong Xing, Song Min *et al. Journal of Nuclear Materials*[J], 2020, 528: 151 859
26 Xu Xiaoxi, Mu Xingqi, Zhu Chao. *Rare Metal Materials and Engineering*[J], 2020, 49(12): 4005
27 Sun Xun, Zhang Hualei, Li Wei *et al. Nanomaterials*[J], 2020, 10 (1): 59
28 Wang Ruixin, Tang Yu, Li Yongyan *et al. Rare Metal Materials and Engineering*[J], 2020, 49(7): 2417 (in Chinese)
29 Song D H, Kim Y G, Lee J K. *Journal of Korean Power Metallurgy Institute* [J], 2020, 27(1): 52
30 Sarkar A, Wang Q, Schiele A *et al. Advanced Materials*[J], 2019, 31(26): 1 806 236
31 Zhang Y H, Zhuang Y, Hu A *et al. Scripta Materialia*[J], 2017, 130: 96
32 Arfaoui M, Radnoczi G, Kovacs Kis V. *Coatings*[J], 2020, 10(1): 60
33 Dai Chunduo, Luo Hong, Li Jun *et al. Applied Surface Science* [J], 2020, 499: 143 903
34 Semerenko Y A, Natsik V D. *Low Temperatutre Physics*[J], 2020, 46 (1): 92
35 Li Z, Zhao S, Ritchie R O *et al. Progress in Materials Science* [J], 2019, 102: 296

粉末冶金法制备 $Al_xCuFeNiCoCr$ 高熵合金及其性能

江佳阳，杜景红，严继康，张家敏，甘国友
(昆明理工大学 材料科学与工程学院，云南 昆明 650093)

摘　要：采用粉末冶金法制备了 $Al_xCuFeNiCoCr$ 高熵合金。研究了铝含量对合金性能和组织的影响，并讨论了合金制备过程中晶粒性能的变化。结果表明，在球磨过程中合金晶粒细化，且合金晶粒尺寸随 Al 含量的增加而增大。在烧结过程中，合金中会产生新的晶粒，并首先吸收一定热量形成含 Al 的金属间化合物。在 1200 ℃加热 2 h 后，获得具有简单晶体结构的相，证实了高熵合金的形成。根据获得的能谱，合金组成均匀，合金化程度高。然而，随着 Al 含量的增加，出现了少量具有高 Al 含量的高对比度区域。合金具有良好的高温抗氧化性能和抗电化学腐蚀性能。随着铝含量的增加，合金的高温抗氧化性能提高。当 Al 含量为 1mol%时，自腐蚀电压为−235 mV。随着 Al 含量的增加，硬度也增加。结果表明，当 Al 含量为 1mol%时，合金具有最佳综合性能。

关键词：高熵合金；粉末冶金；电化学

作者简介：江佳阳，男，1995 年生，硕士，昆明理工大学材料科学与工程学院，云南 昆明 650093，E-mail：cldjh@sina.com